Exact transparent boundary condition for the three-dimensional Schrödinger equation in a rectangular cuboid computational domain

R. M. Feshchenko*
P.N. Lebedev Physical Institute of RAS, 53 Leninski Prospekt, Moscow, Russia, 119991

A. V. Popov
Pushkov Institute of Terrestrial Magnetism, Ionosphere and Radiowave Propagation of RAS, Troitsk, Moscow Region, Russia, 142190

(Received 28 June 2013; revised manuscript received 22 September 2013; published 18 November 2013)

We report an exact transparent boundary condition (TBC) on the surface of a rectangular cuboid for the three-dimensional (3D) time-dependent Schrödinger equation. It is obtained as a generalization of the well-known TBC for the 1D Schrödinger equation and of the exact TBC in the rectangular domain for the 3D parabolic wave equation, which we reported earlier. Like all other TBCs, it is nonlocal in time domain and relates the boundary transverse derivative of the wave function at any given time to the boundary values of the same wave function at all preceding times. We develop a discretization of this boundary condition for the implicit Crank-Nicolson finite difference scheme. Several numerical experiments demonstrate evolution of the wave function in free space as well as propagation through a number of 3D spherically symmetrical and asymmetrical barriers, and, finally, scattering off an asymmetrical 3D potential. The proposed boundary condition is simple and robust, and can be useful in computational quantum mechanics when an accurate numerical solution of the 3D Schrödinger equation is required.

DOI: 10.1103/PhysRevE.88.053308 PACS number(s): 02.60.Lj, 31.15.−p, 03.65.−w, 02.70.Bf

I. INTRODUCTION

The time-dependent Schrödinger equation (TDSE) is a basic law of quantum physics. It is used to study the evolution of various atomic and molecular systems, including many problems of solid state physics. Its numerical solution, in the case of a time- and coordinate-dependent compact potential, is usually based on finite difference (FD) schemes, such as the frequently used Crank-Nicolson implicit scheme [1]. One of the problems with any FD method is a need for suitable boundary conditions. This is so because any numerical scheme is necessarily confined to a finite computational domain, while realistic physical problems are often posed in infinite domains and therefore have spatially unbound solutions. Such a boundary condition has to substitute for the infinite physical domain with some quantitative relations between the wave function values at the artificial boundary. This problem has been intensively studied in computational optics [2] and radiophysics for the Leontovich-Fock parabolic wave (Fresnel) equation—an exact analog of TDSE [3].

A bold and physically clear concept is aimed at a fully transparent (nonreflective) boundary condition (TBC), allowing any wave that reaches a boundary from inside of the computational domain to propagate outward and never return, in other words, providing zero reflection from the domain's boundary. As the way to achieve this ambitious goal sometimes is not straightforward, other types of boundary conditions such as periodic, rigid-wall, and absorptive conditions [4], though not exact and not quite satisfactory, still are widely used in computational quantum mechanics. For the two-dimensional (2D) parabolic wave equation in free space, equivalent to the 1D Schrödinger equation, such a TBC was formulated more than 20 years ago and now is known in several forms, including the Basakov-Popov-Papadakis (BPP) [3,5,6] and Schmidt-Deuflhard-Yevick (SDY) formulations [7]. The SDY condition was specifically tailored for an implicit FD implementation and is unconditionally stable [7]. These TBCs have been extensively used for the 1D Schrödinger equation as well [8,9]. Transparent boundary conditions are generally not local and sometimes rather complicated. They relate the transversal boundary derivative of the wave function at the current spatial point or time to the boundary values of the wave function at all previous times or spatial points [3].

For TDSEs of higher dimensions, the results have been much more limited so far. There exist known transparent boundary conditions on the circular and spherical boundaries in the 2D and 3D spaces, respectively [3,10,11]; see also [6]. There is also a TBC on a straight artificial boundary or plane, which, however, is not suitable for practical calculations [3,9]. Unfortunately, in the 2D and 3D cases, no exact TBCs have been known for a rectangular or rectangular cuboid computational domain (RCCD) (and generally for hyperrectangular domains in d-dimensional space), respectively, which are the most convenient domains in practice. The most serious problem encountered in a general hyperrectangular computational domain is the treatment of the corners (vertices).

In our previous paper, we reported an exact transparent boundary condition in the rectangular domain for the 3D parabolic wave equation [12], which is equivalent to the 2D TDSE. Here we report an exact 3D transparent boundary condition for the 3D Schrödinger equation in the RCCD. Like its 2D predecessor, it relates the boundary transversal derivative of the wave function at any given time to the boundary values of the wave function and the values of a specially constructed auxiliary function at all previous times. The validity and usefulness of the proposed condition is demonstrated by a series of numerical experiments of a particle propagating in free space as well as propagation through various three-dimensional symmetrical and asymmetrical potential barriers or scattering by compact 3D potentials.

*rusl@sci.lebedev.ru

II. DERIVATION OF BOUNDARY CONDITION

A. One-dimensional case

It is useful for further understanding to derive the transparent boundary condition for the 1D Schrödinger equation [12]:

$$i\frac{\partial\psi}{\partial t}+\frac{\partial^2\psi}{\partial x^2}=0. \tag{1}$$

Here, ψ is the wave function, t is time, and x is the spatial coordinate. Let the computational domain be defined as $|x|<a$. It is assumed that the wave function ψ satisfies Eq. (1) outside the computational domain including its boundary. Let it also satisfy an initial condition $\psi(t=0,x)=\psi_0(x)$, where $\psi_0(x)\equiv 0$ for $|x|\geqslant a$. Generalization to the case when ψ_0 is not zero is possible as well [6]. The transparent boundary condition can be obtained in the following way. First, the Laplace transform with respect to time is applied to (1):

$$ipF(p)+\frac{\partial^2F(p)}{\partial x^2}=0. \tag{2}$$

Here p is the Laplace conjugate variable. It was taken into account that $\psi_0(x)=0$ when $|x|\geqslant a$. Equation (2) has two linearly independent solutions; the first one corresponds to the waves propagating from inside of the computational domain, and the second one corresponds to the waves propagating from outside. The latter solution should be neglected because it is assumed that all sources of the initial and diffracted waves are inside the computational domain. For the upper boundary, at $x=a$, the required solution is proportional to $\exp(i\sqrt{ip}x)$, and for the lower boundary, at $x=-a$, it is proportional to $\exp(-i\sqrt{ip}x)$. Using the inverse Laplace transform, one can see that

$$\psi(t,x)=\frac{1}{2\pi i}\int_{c-i\infty}^{c+i\infty}\exp(pt)C^{\pm}(p)\exp(\pm i\sqrt{ip}x)\,dp, \tag{3}$$

where $C^{\pm}(p)$ are some functions depending on the whole field structure inside the computational domain. Now, taking the derivative with respect to x of (3) and setting $x=\pm a$, we obtain

$$\begin{aligned}\frac{\partial\psi}{\partial x}&=\pm\frac{i\sqrt{i}}{2\pi i}\int_{c-i\infty}^{c+i\infty}\exp(pt)\sqrt{p}C^{\pm}(p)\exp(i\sqrt{ip}x)dp\\&=\pm\frac{i\sqrt{i}}{2\pi i}\frac{\partial}{\partial t}\int_{c-i\infty}^{c+i\infty}\exp(pt)\frac{1}{\sqrt{p}}C^{\pm}(p)\exp(i\sqrt{ip}x)dp\\&=\mp\sqrt{\frac{1}{\pi i}}\frac{\partial}{\partial t}\int_0^t\frac{\psi(\zeta,\pm a)}{\sqrt{t-\zeta}}d\zeta.\end{aligned} \tag{4}$$

In this derivation, the convolution property of the Laplace transform has been used. The boundary condition (4) is known as the Basakov-Popov-Papadakis TBC [7]. Note that the functions $C^{\pm}(p)$ disappear, which means that condition (4) holds for an arbitrary structure of the wave function, initial value, and potential inside the computational domain.

B. 3D boundary condition on a plane border

As the next step, a 3D TBC for a planar artificial boundary will be derived. The 3D TDSE that we are concerned with in this paper can be written as

$$i\frac{\partial\psi}{\partial t}+\frac{\partial^2\psi}{\partial x^2}+\frac{\partial^2\psi}{\partial y^2}+\frac{\partial^2\psi}{\partial z^2}-U(x,y,z)\psi=0, \tag{5}$$

where x, y, and z are coordinates and U is a potential. We will generally assume that the potential has a compact support, i.e., that it falls to zero outside a compact computational domain and on its boundary, although, if potential U has a noncompact part that does not depend on spatial coordinates, it is possible by an appropriate gauge transformation to reduce Eq. (5) to one with a compact potential. So, for a compact potential, Eq. (5) outside the computational domain and at its border is

$$i\frac{\partial\psi}{\partial t}+\frac{\partial^2\psi}{\partial x^2}+\frac{\partial^2\psi}{\partial y^2}+\frac{\partial^2\psi}{\partial z^2}=0. \tag{6}$$

Let us define a planar boundary as $x=\pm a$, which will serve as a boundary of the computational domain. The initial values of ψ at $t=0$ for $|x|\geqslant a$ are equal to zero. In order to obtain a TBC for this 3D problem, we apply Fresnel transform to the wave function ψ in the half space defined by $x\geqslant a$ or $x\leqslant -a$:

$$\begin{aligned}\Psi(t,\mu,\nu,x,y,z)=\int_{-\infty}^{+\infty}\int_{-\infty}^{+\infty}&\psi(t,x,\eta,\zeta)\Gamma(\mu-t,y-\eta)\\&\times\Gamma(\nu-t,z-\zeta)\,d\eta d\zeta,\end{aligned} \tag{7}$$

where

$$\Gamma(s,p)=\sqrt{\frac{i}{4\pi s}}\exp\left(i\frac{p^2}{4s}\right),$$

Ψ is an auxiliary function of six variables, and Γ is the propagator of the 1D TDSE, which itself satisfies the 1D TDSE. By definition, function Ψ satisfies Eq. (1) separately for pairs of variables (μ,y) and (ν,z):

$$i\frac{\partial\Psi}{\partial\mu}+\frac{\partial^2\Psi}{\partial y^2}=0, \tag{8}$$

$$i\frac{\partial\Psi}{\partial\nu}+\frac{\partial^2\Psi}{\partial z^2}=0. \tag{9}$$

For the derivative $\partial\Psi/\partial t$, one can prove, using integration by parts, definition (7), and Eqs. (6), (8), and (9), that

$$\begin{aligned}i\frac{\partial\Psi}{\partial t}=&\,i\int_{-\infty}^{+\infty}\int_{-\infty}^{+\infty}\frac{\partial\psi(t,x,\eta,\zeta)}{\partial t}\Gamma(\mu-t,y-\eta)\Gamma(\nu-t,z-\zeta)d\eta d\zeta\\&+i\int_{-\infty}^{+\infty}\int_{-\infty}^{+\infty}\psi(t,x,\eta,\zeta)\frac{\partial\Gamma(\mu-t,y-\eta)}{\partial t}\Gamma(\nu-t,z-\zeta)d\eta d\zeta\\&+i\int_{-\infty}^{+\infty}\int_{-\infty}^{+\infty}\psi(t,x,\eta,\zeta)\Gamma(\mu-t,y-\eta)\frac{\partial\Gamma(\nu-t,z-\zeta)}{\partial t}d\eta d\zeta\end{aligned}$$

$$
\begin{aligned}
&= -i\int_{-\infty}^{+\infty}\psi(t,x,\eta,\zeta)\frac{\partial\Gamma(\mu-t,y-\eta)}{\partial\mu}\Gamma(\nu-t,z-\zeta)d\eta d\zeta\\
&\quad - i\int_{-\infty}^{+\infty}\int_{-\infty}^{+\infty}\psi(t,x,\eta,\zeta)\Gamma(\mu-t,y-\eta)\frac{\partial\Gamma(\nu-t,z-\zeta)}{\partial\nu}d\eta d\zeta\\
&\quad - \int_{-\infty}^{+\infty}\frac{\partial^2\psi(\mu,x,\eta,\zeta)}{\partial x^2}\Gamma(\mu-t,y-\eta)\Gamma(\nu-t,z-\zeta)d\eta d\zeta\\
&\quad - \int_{-\infty}^{+\infty}\int_{-\infty}^{+\infty}\frac{\partial^2\psi(\mu,x,\eta,\zeta)}{\partial\eta^2}\Gamma(\mu-t,y-\eta)\Gamma(\nu-t,z-\zeta)d\eta d\zeta\\
&\quad - \int_{-\infty}^{+\infty}\int_{-\infty}^{+\infty}\frac{\partial^2\psi(\mu,x,\eta,\zeta)}{\partial\zeta^2}\Gamma(\mu-t,y-\eta)\Gamma(\nu-t,z-\zeta)d\eta d\zeta\\
&= -i\frac{\partial\Psi}{\partial\mu} - i\frac{\partial\Psi}{\partial\nu} - \frac{\partial^2\Psi}{\partial x^2} - \frac{\partial^2\Psi}{\partial y^2} - \frac{\partial\Psi}{\partial z^2} = -\frac{\partial^2\Psi}{\partial x^2}. \qquad (10)
\end{aligned}
$$

So, the function Ψ also satisfies Schrödinger equation (1) relative to pair (t,x):

$$i\frac{\partial\Psi}{\partial t} + \frac{\partial^2\Psi}{\partial x^2} = 0. \qquad (11)$$

From definition (7), the limiting relation follows as well,

$$\Psi(t,t,t,x,y,z) = \psi(t,x,y,z). \qquad (12)$$

In each of the Eqs. (8), (9), and (11), Ψ is considered as a function of two variables: t and x, μ and y, or ν and z, respectively, depending only parametrically on the remaining variables. This property makes the derivation of the TBC for a planar boundary fairly straightforward. Using Eq. (1) and condition (4), we can state that at $x = \pm a$, function Ψ satisfies a similar TBC:

$$\frac{\partial\Psi}{\partial x} = \mp\sqrt{\frac{1}{\pi i}}\frac{\partial}{\partial t}\int_0^t\frac{\Psi(\tau,\mu,\nu,\pm a,y,z)}{\sqrt{t-\tau}}d\tau. \qquad (13)$$

Now, taking into account (12), the following condition at $x = \pm a$ for the function ψ can be obtained:

$$\frac{\partial\psi}{\partial x} = \mp\sqrt{\frac{1}{\pi i}}\frac{\partial}{\partial t}\int_0^t\frac{\Psi(\tau,\mu,\nu,\pm a,y,z)}{\sqrt{t-\tau}}d\tau\Bigg|_{t=\mu=\nu}. \qquad (14)$$

The function $\Psi(\tau,\mu,\nu,x,y,z)$ in the plane $x = \pm a$ at $t = \mu = \nu$ can be found by solving Eqs. (8) and (9) or an equivalent 2D TDSE:

$$
\begin{aligned}
&i\frac{\partial\Psi(\tau,t,t,\pm a,y,z)}{\partial t} + \frac{\partial^2\Psi(\tau,t,t,\pm a,y,z)}{\partial y^2}\\
&\quad + \frac{\partial^2\Psi(\tau,t,t,\pm a,y,z)}{\partial z^2} = 0. \qquad (15)
\end{aligned}
$$

The identity (12) serves as the initial condition. The solution of (15) can be done numerically with a FD scheme supplemented with a similar transparent 2D TBC (see [12]) at the boundaries at $y = \pm b$ and $z = \pm c$ in the plane $x = \pm a$.

C. 3D boundary condition in rectangular cuboid domain

Let us now consider a computational domain defined as

$$|x| < a, \quad |y| < b, \quad |z| < c. \qquad (16)$$

In the (x,y,z) space, the domain is a rectangular cuboid. Its projections on the (x,y), (y,z), and (x,z) planes are rectangles. On each of the six lateral facets of the cuboid, the boundary condition of the (14) type is valid because all six facets are parts of infinite planes. Evaluation of the function $\Psi(t,\mu,\nu,x,y,z)$ on the facets using Eq. (15) involves TBCs at the edges of the cuboid. It means that in order to impose a transparent boundary condition on the functions $\Psi(\tau,t,t,\pm a,y,z)$, $\Psi(t,\mu,t,x,\pm b,z)$, or $\Psi(t,t,\nu,x,y,\pm c)$, one needs to know the values of Ψ at the cuboid's 12 edges $\Psi(\tau,\mu,t,\pm a,\pm b,z)$, $\Psi(t,\mu,\nu,x,\pm b,\pm c)$, or $\Psi(\tau,t,\nu,\pm a,y,\pm c)$, which, in turn, can be found by solution of type (1) equations with transparent boundary conditions formulated at the eight vertices of the cuboid $\Psi(\tau,\mu,\nu,\pm a,\pm b,\pm c)$.

Below we describe a simple and efficient code implementing this boundary condition.

III. NUMERICAL IMPLEMENTATION

A. Finite difference scheme

We look for a numerical solution of the 3D Schrödinger equation (5) inside a finite computational domain. The potential energy U is supposed to vanish outside the computational domain and at its boundary, where Eq. (5) reduces to (6). At the initial time $t = 0$, the wave function takes a compact initial value $\psi = \psi_0(x,y,z)$. To solve this boundary value problem, we use the standard Crank-Nicolson scheme [1].

There exist, of course, different numerical schemes, which can be used to solve parabolic type equations, such as the alternating direction implicit method [13], a very efficient Chebyshev expansion of the time evolution operator method [14], and generalized Crank-Nicolson methods [15]. The first of them—alternating direction implicit method—is actually a perfect match to the boundary condition considered in the present paper, as both involve splitting the initial multidimensional equation into a number of one-dimensional equations. Still we chose the Crank-Nicolson scheme but only as a way to show that the multidimensional transparent boundary condition is compatible with this standard and widely used FD scheme. Other methods may be used in our future works.

The computational grid is defined as follows. For simplicity, we assume that $a = b = c$. A generalization to the case when $a \neq b \neq c$ is trivial. The computational step along all spatial axes is $h = 2a/N$, where $N + 1$ is the number of grid nodes in the x, y, and z direction. The total number of spatial nodes is $(N+1)^3 - 12(N-1) - 8$, as the eight vertices and 12 edges are excluded. The time step length is τ. The number of t steps is N_τ. The Crank-Nicolson approximation to (5) can be written as

$$
\begin{aligned}
-i\frac{\psi^{n+1}_{m,s,p} - \psi^{n}_{m,s,p}}{\tau} = &-\frac{U^{n+1}_{m,s,p}\psi^{n+1}_{m,s,p} + U^{n}_{m,s,p}\psi^{n}_{m,s,p}}{2} + \frac{\psi^{n+1}_{m+1,s,p} - 2\psi^{n+1}_{m,s,p} + \psi^{n+1}_{m-1,s,p}}{2h^2} + \frac{\psi^{n}_{m+1,s,p} - 2\psi^{n}_{m,s,p} + \psi^{n}_{m-1,s,p}}{2h^2} \\
&+ \frac{\psi^{n+1}_{m,s+1,p} - 2\psi^{n+1}_{m,s,p} + \psi^{n+1}_{m,s-1,p}}{2h^2} + \frac{\psi^{n}_{m,s+1,p} - 2\psi^{n}_{m,s,p} + \psi^{n}_{m,s-1,p}}{2h^2} + \frac{\psi^{n+1}_{m,s,p+1} - 2\psi^{n+1}_{m,s,p} + \psi^{n+1}_{m,s,p-1}}{2h^2} \\
&+ \frac{\psi^{n}_{m,s,p+1} - 2\psi^{n}_{m,s,p} + \psi^{n}_{m,s,p-1}}{2h^2}, \qquad (17)
\end{aligned}
$$

where

$$
\begin{aligned}
\psi^{n}_{m,s,p} &= \psi(\tau n, hm, hs, hp), \\
U^{n}_{m,s,p} &= U(\tau n, hm, hs, hp), \\
0 \leqslant n \leqslant N_\tau,&\quad 1 \leqslant m,s,p \leqslant N-1,
\end{aligned}
$$

and n is the current marching step. There is a total of $(N-1)^3$ equations in Eq. (17). After a simplification, they become

$$
\begin{aligned}
&-\psi^{n+1}_{m+1,s,p} - \psi^{n+1}_{m,s+1,p} - \psi^{n+1}_{m,s,p+1} + C^{n+1}_{m,s,p}\psi^{n+1}_{m,s,p} - \psi^{n+1}_{m-1,s,p} - \psi^{n+1}_{m,s-1,p} - \psi^{n+1}_{m,s,p-1} \\
&= \psi^{n}_{m+1,s,p} + \psi^{n}_{m,s+1,p} + \psi^{n}_{m,s,p+1} - \tilde{C}^{n}_{m,s,p}\psi^{n}_{m,s,p} + \psi^{n}_{m-1,s,p} + \psi^{n}_{m,s-1,p} + \psi^{n}_{m,s,p-1}, \qquad (18)
\end{aligned}
$$

where

$$
C^{n}_{m,s,p} = 6 + h^2 U^{n}_{m,s,p} - 2ih^2/\tau, \qquad (19)
$$

$$
\tilde{C}^{n}_{m,s,p} = 6 + h^2 U^{n}_{m,s,p} + 2ih^2/\tau. \qquad (20)
$$

The boundaries of the computational domain are located at $m,s,p = N-1$ and $m,s,p = 1$. Transparent boundary conditions in the form of (14) can be expressed in finite differences as

$$
\frac{\psi^{n+1}_{N,s,p} - \psi^{n+1}_{N-2,s,p}}{2h} + 2\sigma\left(\psi^{n+1}_{N-1,s,p} - \sum_{l=1}^{n}\gamma_l \Psi^{n+1-l,n+1,n+1}_{N-1,s,p}\right) = 0, \quad x = a, \qquad (21)
$$

$$
\frac{\psi^{n+1}_{2,s,p} - \psi^{n+1}_{0,s,p}}{2h} - 2\sigma\left(\psi^{n+1}_{1,s,p} - \sum_{l=1}^{n}\gamma_l \Psi^{n+1-l,n+1,n+1}_{1,s,p}\right) = 0, \quad x = -a, \qquad (22)
$$

$$
\frac{\psi^{n+1}_{m,N,p} - \psi^{n+1}_{m,N-2,p}}{2h} + 2\sigma\left(\psi^{n+1}_{m,N-1,p} - \sum_{l=1}^{n}\gamma_l \Psi^{n+1,n+1-l,n+1}_{m,N-1,p}\right) = 0, \quad y = a, \qquad (23)
$$

$$
\frac{\psi^{n+1}_{m,2,p} - \psi^{n+1}_{m,0,p}}{2h} - 2\sigma\left(\psi^{n+1}_{m,1,p} - \sum_{l=1}^{n}\gamma_l \Psi^{n+1,n+1-l,n+1}_{m,1,p}\right) = 0, \quad y = -a, \qquad (24)
$$

$$
\frac{\psi^{n+1}_{m,s,N} - \psi^{n+1}_{m,s,N-2}}{2h} + 2\sigma\left(\psi^{n+1}_{m,s,N-1} - \sum_{l=1}^{n}\gamma_l \Psi^{n+1,n+1,n+1-l}_{m,s,N-1}\right) = 0, \quad z = a, \qquad (25)
$$

$$
\frac{\psi^{n+1}_{m,s,2} - \psi^{n+1}_{m,s,0}}{2h} - 2\sigma\left(\psi^{n+1}_{m,s,1} - \sum_{l=1}^{n}\gamma_l \Psi^{n+1,n+1,n+1-l}_{m,s,1}\right) = 0, \quad z = -a, \qquad (26)
$$

where [5]

$$
\begin{aligned}
\gamma_l &= \frac{2}{(\sqrt{l+1} + \sqrt{l})(\sqrt{l} + \sqrt{l-1})(\sqrt{l+1} + \sqrt{l-1})}, \\
\sigma &= \frac{1}{\sqrt{i\pi\tau}}, \\
\Psi^{n,q,r}_{m,s,p} &= \Psi(\tau n, \tau q, \tau r, hm, hs, hp), \quad \psi^{n}_{m,s,p} = \Psi^{n,n,n}_{m,s,p}.
\end{aligned}
$$

The normal derivatives at the boundaries are calculated in the second order approximation as differences between the values of wave function at $m,s,p = 2$ and $m,s,p = 0$ or $m,s,p = N$ and $m,s,p = N-2$, respectively. Conditions (21) and (22) hold for the facets at $x = \pm a$, while conditions (23)–(26) are for those at $y = \pm a$ and $z = \pm a$, respectively. The discretized boundary conditions shown above, as well as conditions (37)–(39) and (41)–(43) below, were obtained using the trapezoidal quadrature

rule for the integral in Eq. (14) with subsequent numerical differentiation (see [5] and Eq. (3.7) in Ref. [3]). The function ψ appears in the sum in parentheses due to (12). There is a total of $6(N-1)^2$ equations in Eqs. (21)–(26). Together with Eq. (17), there are a total of $(N-1)^3+6(N-1)^2=(N+1)^3-12(N-1)-8$ equations, which is equal to the number of grid nodes in Eq. (17). It is worth mentioning that in the 1D case, the discretization (21)–(26) has been found to be unconditionally stable [3].

The auxiliary function Ψ on the facets is governed by differential equation (15), which also can be approximated by a Crank-Nicolson FD scheme. For instance, on the facet at $x=a$ ($m=N-1$), the FD equations are

$$\begin{aligned}&-\Psi^{q,n+1,n+1}_{N-1,s+1,p}-\Psi^{q,n+1,n+1}_{N-1,s,p+1}+D\Psi^{q,n+1,n+1}_{N-1,s,p}-\Psi^{q,n+1,n+1}_{N-1,s-1,p}-\Psi^{q,n+1,n+1}_{N-1,s,p-1}\\&\quad=\Psi^{q,n,n}_{N-1,s+1,p}+\Psi^{q,n,n}_{N-1,s,p+1}-\tilde{D}\Psi^{q,n,n}_{N-1,s,p}+\Psi^{q,n,n}_{N-1,s-1,p}+\Psi^{q,n,n}_{N-1,s,p-1},\end{aligned}\tag{27}$$

where

$$D=4-2ih^2/\tau,\quad \tilde{D}=4+2ih^2/\tau,\quad 0\leqslant q\leqslant n.$$

Equations similar to (27) can be written for the remaining five facets. They express the function $\Psi^{q,n+1,n+1}_{N-1,s,p}$ for each q in terms of function $\Psi^{q,n,n}_{N-1,s,p}$ from the previous computational step n. So, there are a total of six 3D arrays $N^2\times n$ corresponding to the six facets that need to be stored for use at the $n+1$ computational step.

Equations (27) should be solved with the following transparent boundary conditions at the four edges at $y=\pm a$ and $z=\pm a$, which are fully analogous to (21)–(26):

$$\frac{\Psi^{q,n+1,n+1}_{N-1,N,p}-\Psi^{q,n+1,n+1}_{N-1,N-2,p}}{2h}+2\sigma\left(\Psi^{q,n+1,n+1}_{N-1,N-1,p}-\sum_{l=1}^{n}\gamma_l\Psi^{q,n+1-l,n+1}_{N-1,N-1,p}\right)=0,\quad y=a,\tag{28}$$

$$\frac{\Psi^{q,n+1,n+1}_{N-1,2,p}-\Psi^{q,n+1,n+1}_{N-1,0,p}}{2h}-2\sigma\left(\Psi^{q,n+1,n+1}_{N-1,1,p}-\sum_{l=1}^{n}\gamma_l\Psi^{n+1,n+1-l,n+1}_{N-1,1,p}\right)=0,\quad y=-a,\tag{29}$$

$$\frac{\Psi^{q,n+1,n+1}_{N-1,s,N}-\Psi^{q,n+1,n+1}_{N-1,s,N-2}}{2h}+2\sigma\left(\Psi^{q,n+1,n+1}_{N-1,s,N-1}-\sum_{l=1}^{n}\gamma_l\Psi^{n+1,n+1,n+1-l}_{N-1,s,N-1}\right)=0,\quad z=a,\tag{30}$$

$$\frac{\Psi^{q,n+1,n+1}_{N-1,s,2}-\Psi^{q,n+1,n+1}_{N-1,s,0}}{2h}-2\sigma\left(\Psi^{q,n+1,n+1}_{N-1,s,1}-\sum_{l=1}^{n}\gamma_l\Psi^{n+1,n+1,n+1-l}_{N-1,s,1}\right)=0,\quad z=-a.\tag{31}$$

The Ψ function on the facet's edges from (28)–(31) can be found, in turn, by solving Eqs. (8) or (9) with the following FD schemes:

$$-\Psi^{q,r,n+1}_{N-1,N-1,p+1}+B\Psi^{q,r,n+1}_{N-1,N-1,p}-\Psi^{q,r,n+1}_{N-1,N-1,p-1}=\Psi^{q,r,n}_{N-1,N-1,p+1}-\tilde{B}\Psi^{q,r,n}_{N-1,N-1,p}+\Psi^{q,r,n}_{N-1,N-1,p-1},\tag{32}$$

$$-\Psi^{q,r,n+1}_{N-1,1,p+1}+B\Psi^{q,r,n+1}_{N-1,1,p}-\Psi^{q,r,n+1}_{N-1,1,p-1}=\Psi^{q,r,n}_{N-1,1,p+1}-\tilde{B}\Psi^{q,r,n}_{N-1,1,p}+\Psi^{q,r,n}_{N-1,1,p-1},\tag{33}$$

$$-\Psi^{q,n+1,r}_{N-1,s+1,N-1}+B\Psi^{q,n+1,r}_{N-1,s,N-1}-\Psi^{q,n+1,r}_{N-1,s-1,N-1}=\Psi^{q,n,r}_{N-1,s+1,N-1}-\tilde{B}\Psi^{q,n,r}_{N-1,s,N-1}+\Psi^{q,n,r}_{N-1,s-1,N-1},\tag{34}$$

$$-\Psi^{q,n+1,r}_{N-1,s+1,1}+B\Psi^{q,n+1,r}_{N-1,s,1}-\Psi^{q,n+1,r}_{N-1,s-1,1}=\Psi^{q,n,r}_{N-1,s+1,1}-\tilde{B}\Psi^{q,n,r}_{N-1,s,1}+\Psi^{q,n,r}_{N-1,s-1,1},\tag{35}$$

where

$$B=2-2ih^2/\tau,\quad \tilde{B}=2+2ih^2/\tau,\quad 0\leqslant q,\quad r\leqslant n.$$

Similar to the 2D equations above, formulas (32)–(35) express functions $\Psi^{q,r,n+1}_{N-1,N-1,p}$, $\Psi^{q,r,n+1}_{N-1,1,p}$, $\Psi^{q,n+1,r}_{N-1,s,N-1}$, and $\Psi^{q,n+1,r}_{N-1,s,1}$ for each q,r via the functions $\Psi^{q,r,n}_{N-1,N-1,p}$, $\Psi^{q,r,n}_{N-1,1,p}$, $\Psi^{q,n,r}_{N-1,s,N-1}$, and $\Psi^{q,n,r}_{N-1,s,1}$ from the previous computational step n, respectively. So, there are a total of 12 3D "edge" arrays $N\times n^2$ that need to be stored for use at the $n+1$ computational step.

The TBCs for Eqs. (32) and (33) are as follows:

$$\frac{\Psi^{q,r,n+1}_{N-1,N-1,N}-\Psi^{q,r,n+1}_{N-1,N-1,N-2}}{2h}+2\sigma\left(\Psi^{q,r,n+1}_{N-1,N-1,N-1}-\sum_{l=1}^{n}\gamma_l\Psi^{q,r,n+1-l}_{N-1,N-1,N-1}\right)=0,\quad y=a,\quad z=a,\tag{36}$$

$$\frac{\Psi^{q,r,n+1}_{N-1,N-1,2}-\Psi^{q,r,n+1}_{N-1,N-1,0}}{2h}-2\sigma\left(\Psi^{q,r,n+1}_{N-1,N-1,1}-\sum_{l=1}^{n}\gamma_l\Psi^{q,r,n+1-l}_{N-1,N-1,1}\right)=0,\quad y=a,\quad z=-a,\tag{37}$$

$$\frac{\Psi^{q,r,n+1}_{N-1,1,N}-\Psi^{q,r,n+1}_{N-1,1,N-2}}{2h}+2\sigma\left(\Psi^{q,r,n+1}_{N-1,1,N-1}-\sum_{l=1}^{n}\gamma_l\Psi^{q,r,n+1-l}_{N-1,1,N-1}\right)=0,\quad y=-a,\quad z=a,\tag{38}$$

$$\frac{\Psi^{q,r,n+1}_{N-1,1,2}-\Psi^{q,r,n+1}_{N-1,1,0}}{2h}-2\sigma\left(\Psi^{q,r,n+1}_{N-1,1,1}-\sum_{l=1}^{n}\gamma_l\Psi^{q,r,n+1-l}_{N-1,1,1}\right)=0,\quad y=-a,\quad z=-a.\tag{39}$$

Similarly, for Eqs. (34) and (35), the boundary conditions are

$$\frac{\Psi^{q,n+1,r}_{N-1,N,N-1}-\Psi^{q,n+1,r}_{N-1,N-2,N-1}}{2h}+2\sigma\left(\Psi^{q,n+1,r}_{N-1,N-1,N-1}-\sum_{l=1}^{n}\gamma_l\Psi^{q,n+1-l,r}_{N-1,N-1,N-1}\right)=0,\quad y=a,\quad z=a, \tag{40}$$

$$\frac{\Psi^{q,n+1,r}_{N-1,2,N-1}-\Psi^{q,n+1,r}_{N-1,0,N-1}}{2h}-2\sigma\left(\Psi^{q,n+1,r}_{N-1,1,N-1}-\sum_{l=1}^{n}\gamma_l\Psi^{q,n+1-l,r}_{N-1,1,N-1}\right)=0,\quad y=-a,\quad z=a, \tag{41}$$

$$\frac{\Psi^{q,n+1,r}_{N-1,N,1}-\Psi^{q,n+1,r}_{N-1,N-2,1}}{2h}+2\sigma\left(\Psi^{q,n+1,r}_{N-1,N-1,1}-\sum_{l=1}^{n}\gamma_l\Psi^{q,n+1-l,r}_{N-1,N-1,1}\right)=0,\quad y=a,\quad z=-a, \tag{42}$$

$$\frac{\Psi^{q,n+1,r}_{N-1,2,1}-\Psi^{q,n+1,r}_{N-1,0,1}}{2h}-2\sigma\left(\Psi^{q,n+1,r}_{N-1,1,1}-\sum_{l=1}^{n}\gamma_l\Psi^{q,n+1-l,r}_{N-1,1,1}\right)=0,\quad y=-a,\quad z=-a. \tag{43}$$

There are a total of eight 3D "vertex" n^3 arrays in the boundary conditions (36)–(43) that need to be stored for use at the $n+1$ computational step.

All equations (18), (21)–(43) and similar equations on the other five facets and eight edges should be solved together in the following order:

(1) At the first stage, Eqs. (32)–(35) and similar equations on the other eight edges are used to evaluate the auxiliary function Ψ on each edge of the computational domain and for each q and r from step n to step $n+1$ using the stored values from the previous computational step and the stored boundary values at the vertices $\Psi^{q,r,v}_{N-1,N-1,N-1}$, $\Psi^{q,r,v}_{N-1,N-1,1}$, $\Psi^{q,r,v}_{N-1,1,N-1}$, and $\Psi^{q,r,v}_{N-1,1,1}$ in TBCs (36)–(43).

(2) At the next stage, Eqs. (27) and similar equations on the other five facets are used to propagate the auxiliary function Ψ on each facet of the computational domain and for each q from step n to step $n+1$ using the stored values from the previous computational step and the boundary values at the edges $\Psi^{q,r,n+1}_{N-1,N-1,p}$, $\Psi^{q,r,n+1}_{N-1,1,p}$, $\Psi^{q,r,n+1}_{N-1,s,N-1}$, and $\Psi^{q,r,n+1}_{N-1,s,1}$ (found at stage 1) in TBCs (28)–(31).

(3) At the third stage, the obtained values of the auxiliary function Ψ at the boundary of the computational domain are used in the boundary conditions (21)–(24). Now the equation sets (17), (21)–(24) can be solved, thus propagating the wave function ψ from the n to $n+1$ step.

(4) The new values of the function Ψ at the artificial boundary are stored. As said above, six $N^2\times n$ arrays contain the auxiliary function Ψ on the facets. Twelve additional $N\times n^2$ arrays store the function Ψ at the edges of the computational domain. Finally, eight n^3 arrays store the function Ψ at the vertices. It is clear that at each marching step, the new values from one facet or edge will be used in the boundary conditions for the auxiliary function in the adjacent facets or edges. Through this mechanism, the ψ fields on different facets and edges influence each other.

The maximum total number of Ψ function values which need to be stored is $6N^2N_\tau+12NN_\tau{}^2+8N_\tau{}^3$.

B. Computational costs and complexity

Let us consider the numerical complexity of the FD scheme at the computational step n. The FD equation set (17) is a sparse linear system. Its solution with a direct sparse solver imposes computational costs proportional to N^6, although in practice a faster iterative solver can be used. The TBCs (21)–(26) entail (for a direct solver) computational costs of the order of $6N^2\times n$. The solution of n 2D equations of (27) type requires about $6N^4\times n$ operations. Implementation of the boundary conditions (28)–(31) takes about $24N\times n^2$ operations. The computation costs associated with (32)–(35) and boundary conditions (36)–(43) are $12N\times n^2$ and $24n^3$, respectively. So, the full complexity (FC) at each step is about

$$\mathrm{FC}\approx P\times N^6+Q\times N\times n^2+R\times N^4\times n+S\times N\times n^2+T\times n^3, \tag{44}$$

where P, Q, R, S, and T are some coefficients. The whole computational burden can be estimated by multiplying this expression by n. It is clear that the first and last terms in the above expression are the main contributors to the computational costs. If n is much smaller than N^2, then the performance of the FD scheme is determined by the sparse solver used. In the opposite case, the boundary condition will dominate. For instance, if $N=100$ (as in some examples below), the threshold n is about 10 000.

This markedly differs from the 1D case where the computational costs per each step are about $P\times N+Q\times n$. In this case, the threshold n, where the boundary condition begins to dominate, is proportional to N. In the 3D (as well as in the 2D) case, the TBC contributes significantly less to the total computational costs per step relative to the 1D case. So, if the number of the grid nodes N in spatial directions is large, the contribution of the boundary condition will be entirely negligible. We emphasize here that in realistic problems, the computational costs will be determined mainly by the number of inner nodes, not by the discretized boundary condition. Therefore, in the sense of performance, the proposed exact nonlocal TBC does not differ much from the commonly used approximate local boundary conditions, such as absorptive boundary conditions. In terms of the required computer memory, the TBC is obviously more burdensome than local boundary conditions, but, as the popular saying goes, "memory is cheap."

One can also note that at each computational step, implementation of the proposed TBC involves solving $6n$ independent 2D equation sets of the (27) type and $12n^2$ systems of the (28)–(31) type, which can be easily parallelized, thus significantly speeding up calculation. Moreover, the numerical costs can be further reduced using well-known speed-up strategies for 1D computations, which form the basis of the

proposed transparent boundary condition, as discussed, for instance, in Ref. [3]. For example, the array of the past boundary values needed to be stored can be truncated because only the values closest to the current step actually influence the solution. So, the above calculations actually overestimate the true computational burden of the proposed TBC.

IV. NUMERICAL EXPERIMENTS

In order to quantitatively assess the accuracy of the proposed TBC, we carried out a number of simple numerical experiments. Some model spherically symmetrical or asymmetrical potentials and initial conditions were considered.

A. Free space evolution

The first numerical experiment simulates evolution of a linear superposition of Gaussian wavelets, which are, in our case, exact solutions of the 3D TDSE in free space. We can compare the analytic representation with the numerical results obtained using the Crank-Nicolson FD scheme with our TBC, as outlined above. The sum of Gaussian wavelets used here has the following form:

$$\psi_g(x,y,z,t) = \sum_{l=1}^{3} \psi_g^l(x,y,z,t), \tag{45}$$

where

$$\psi_g^l(x,y,z,t) = \frac{w_l^3}{\left(w_l^2+4it\right)^{3/2}} \exp\{i\xi_l[(x-t\xi_l\cos\alpha_l)\cos\alpha_l + (y-t\xi_l\cos\beta_l)\cos\beta_l + (z-t\xi_l\cos\gamma_l)\cos\gamma_l]\}$$
$$\times \exp\left\{-[(x-2t\xi_l\cos\alpha_l)^2 + (y-2t\xi_l\cos\beta_l)^2 + (z-2t\xi_l\cos\gamma_l)^2]\Big/\left(w_l^2+4it\right)\right\}. \tag{46}$$

Here, $\cos\alpha_l$, $\cos\beta_l$, and $\cos\gamma_l$ are the directional cosines. The w_l is the waist radius. The ξ_l is a parameter. All parameters, which were chosen arbitrarily, are listed in Table I.

The size of the computational domain was $200 \times 200 \times 200$ (in arbitrary units) with the spatial grid step equal to 4, 3, or 2 in different experiments. The time step was 50, 25, or 20 units, with the number of time steps varying from 80 to 200. In each numerical experiment, the relative differences V and Y between the exact solution (45) and (46) and the FD approximation with the same initial value $[\psi_0(x,y,z) = \psi_g(x,y,z,0)]$ were calculated and plotted as functions of $t = n\tau$. The functions V and Y were defined as

$$V(\tau n) = \sum_{m,s,p=0}^{N} \left|\psi_{m,s,p}^n - \psi_g(\tau n,hm,hs,hp)\right|^2 \Big/ \sum_{m,s,p=0}^{N} |\psi_g(\tau n,hm,hs,hp)|^2, \tag{47}$$

$$Y(\tau n) = \sum_{m,s,p=0}^{N} \left[\left|\psi_{m,s,p}^n\right|^2 - |\psi_g(\tau n,hm,hs,hp)|^2\right] \Big/ \sum_{m,s,p=0}^{N} |\psi_g(\tau n,hm,hs,hp)|^2. \tag{48}$$

The function Y estimates the difference between the exact and approximate total probabilities that the particle is still inside the computational domain. As compared to V, it is independent of phase errors and is quite sensitive to the spurious reflections from the artificial boundary. The function Y is not always positive, whereas V is.

The results for a number of combinations of h, τ and the time range $N_\tau \times \tau = 4000$ are plotted in Figs. 1 and 2 for V and Y, respectively. The peak near $t = 400$ observed in all curves in Fig. 1 (as well as in Fig. 2) is caused by the discretization error of the FD scheme, which gradually increases from zero value at the initial time step. A smaller second peak near $t = 1500$, of the order of $V = 10^{-3}$–10^{-2}, is caused by spurious reflections from the artificial boundary due to the TBC discretization error. After that, all curves

TABLE I. The parameters of Gaussian wavelets used in Eq. (45). The ξ_l parameters were chosen to be on average 0.05, so that the wave packet reaches a vertex at about $t = 1700$.

$\cos\alpha$	$\cos\beta$	$\cos\gamma$	ξ	w (arb. units)
$1/\sqrt{3}$	$1/\sqrt{3}$	$1/\sqrt{3}$	0.05	18
$1/\sqrt{2}$	$1/\sqrt{2}$	0	0.1	18
1	0	0	0.02	18

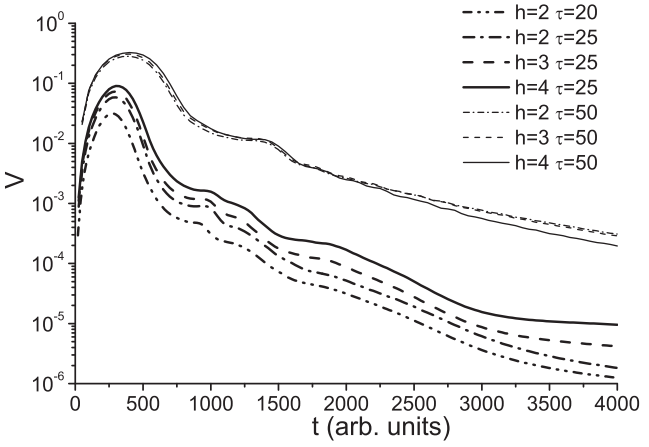

FIG. 1. Evolution of a superposition of Gaussian wavelets (see Table I) in free space. The curves show the difference V [see (47)] between the numerical and exact solutions for a number of values of parameters τ, h.

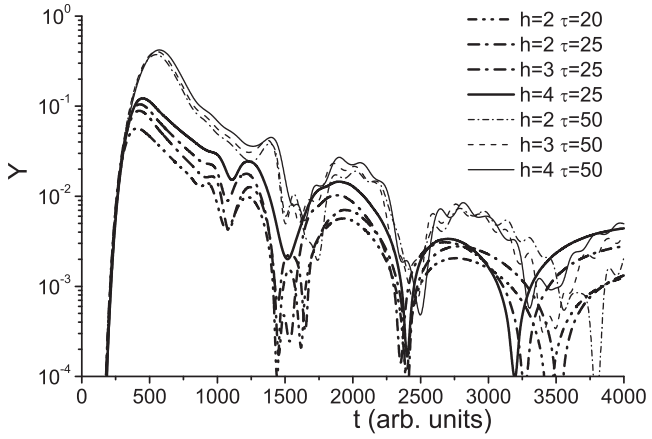

FIG. 2. Evolution of a superposition of Gaussian wavelets (see Table I) in free space. The curves show the difference $|Y|$ [see (48)] between the numerical and exact solutions for a number of values of parameters τ, h.

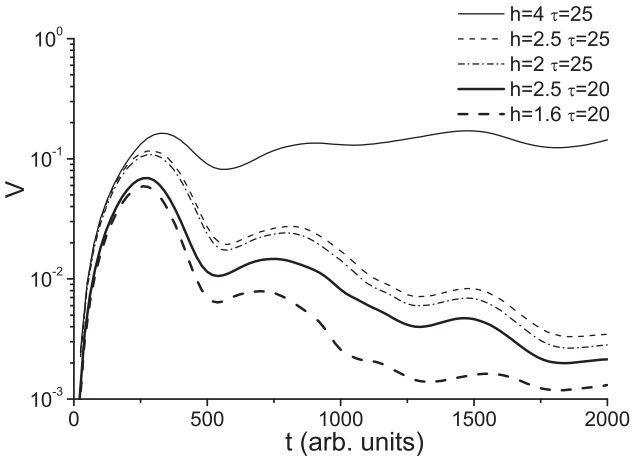

FIG. 3. Propagation of a particle through a spherical barrier with $r_0 = 70$ and $r_1 = 80$. The curves show the difference V between the full 3D simulation and "exact" quasi-1D solution for different h, τ and fixed time range $N_\tau \times \tau = 2000$. In 1D calculations, the grid steps h and τ were a hundred times smaller then those used in the 3D simulation.

monotonically go to zero without any obvious instability. In Fig. 2, the total relative power in spurious reflections from the artificial boundary generally does not exceed 1% and is decreasing with time, which means that the FD scheme together with the TBC is computationally stable.

B. Spherically symmetrical problem

The second numerical experiment simulates a more complicated situation: evolution of a spherically symmetric Gaussian wavelet in a spherically symmetrical potential U and with spherically symmetrical initial conditions. It is well known that in this case, the 3D Schrödinger equation (6), if written in the spherical coordinates, can be reduced to a 1D Schrödinger equation by substitution $\psi = \varphi/r$, where r is the modulus of radius vector,

$$i\frac{\partial\varphi}{\partial t} + \frac{\partial^2\varphi}{\partial r^2} - U(r)\varphi = 0. \tag{49}$$

The 1D equation (49) for $\varphi(r,t)$ can be solved numerically like any other 1D parabolic type equation. The required boundary conditions are a zero boundary condition at $r = 0$ and an exact 1D transparent boundary condition (4) at the outer border. This numerical solution, which can be done using a very dense spatial and temporal grid providing a very high precision, plays the role of an exact solution. On the other hand, the problem can be solved with the proposed fully 3D method being tested. The two solutions, i.e., an "exact" one (ψ_{1D}) and an approximate one, were then compared to each other by calculating their difference V as defined in Eq. (47).

The potential used here was a simple, spherically symmetrical, shell-like barrier with $U = 0$ for $r < r_0$ or $r > r_1$, and $U = 0.01$ for $r_0 < r < r_1$. The size of the computational domain was chosen to be $200 \times 200 \times 200$ units, as before. At the initial moment $t = 0$ and for $r < r_0$, the wave function was assumed to be a Gaussian wavelet (46) with the waist radius of $w = 14$ and $\xi = 0$. For $r > r_0$, the initial wave function was assumed to be zero.

The results of this numerical experiment for various values of h and τ in 3D calculations are plotted in Fig. 3. Like in the previous numerical experiment, the peak in Fig. 3 near $t = 300$ is caused by the discretization error of the FD scheme. Smaller second peaks near $t = 800$ and $t = 1800$ are caused by spurious reflections from the artificial boundary due to the TBC discretization error. After that, all curves except one monotonically go to zero without any obvious instability.

Cross sections of the double logarithm of $|\psi/\psi_{1D}|^2$ in the (x,z) plane for $y = 0$ and four time values are shown in Fig. 4, whereas Fig. 5 shows the same quantity along a space diagonal to the computational domain as a function of time. For the model considered in this section, it is expected that a number of divergent spherical waves will propagate from the central region enclosed by the potential barrier through the artificial boundary of the computational domain. Figures 4 and 5 demonstrate exactly this: the circular and inclined bands, respectively, seen in them are remnants of these leaking divergent waves that are visible because of residual numerical errors of the FD scheme. It can be observed that the waves remain undisturbed, showing no apparent reflections from the artificial boundary. In the dark colored "wings" in Fig. 5 (when $t < 400$), which are also visible in the corners in Fig. 4(a), the relative difference between the numerical and reference solution is large but the ψ field itself is very small. Thus, this large difference is due to numerical noise. Outside these wings, the relative difference is generally quite small: $\sim 10^{-2}$.

C. Nonspherical potentials

We further demonstrate the validity of the derived transparent boundary condition for the TDSE by two toy models. One of them is quantum particle propagating through a nonspherical potential barrier in 3D space, and the second one is backscattering by a nonspherically symmetrical potential. In these simulations, the size of the computational domain was again $200 \times 200 \times 200$ units, whereas other parameters were $h = 1.66$, $\tau = 20$ and $N_\tau * \tau = 2000$. The initial ψ

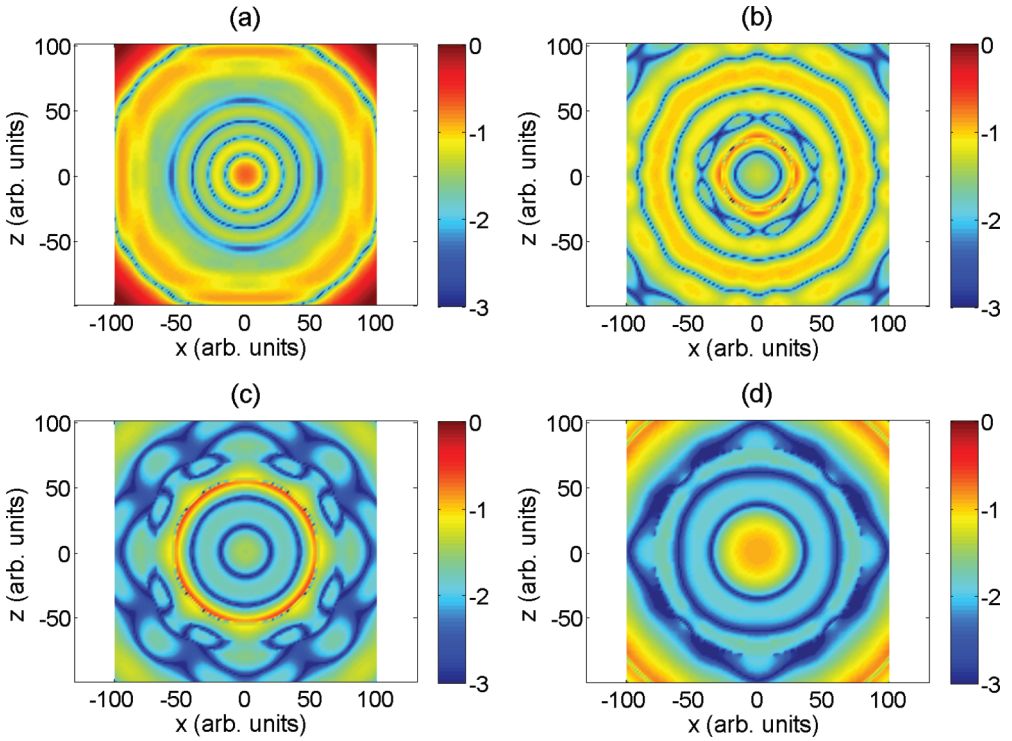

FIG. 4. (Color online) Propagation of a particle through a spherical barrier with $r_0 = 70$ and $r_1 = 80$. Distributions of $\log_{10}|\log_{10}(|\psi/\psi_{1D}|^2)|$ in the (x,z) plane at $y = 0$ are plotted at four different times: (a) -320, (b) -640, (c) -1280, and (d) -1920 arb. units. The parameters of simulation were $\tau = 20$, $h = 1.66$ and $N_\tau * \tau = 2000$. The choice of this particular metrics was motivated by our desire to better emphasize the differences between the reference and approximate solutions.

distribution at $t = 0$ was a Gaussian wavelet (46) with the waist radius of $w = 14$ and $\xi = 0$.

Figure 6 shows successive quantum state densities $|\psi|^2$ in the (x,z) plane for a semispherical shell-like potential with $U = 0$ if $r < r_0$ or $r > r_1$ or $x < 0$, and $U = 0.01$ if $r_0 < r < r_1$ and $x > 0$ (a half of that used in the previous section). Figure 7 shows $|\psi|^2$ in the (x,z) plane for a semispherical well-like potential with $U = 0$ when $r > r_0$ or $x < 0$, and $U = -0.01$ if $r < r_0$ and $x > 0$.

In the first example, the semishell acts like a concave mirror, reflecting and focusing a fraction of the ψ field in the negative x direction. This can be clearly seen in Fig. 6(b)

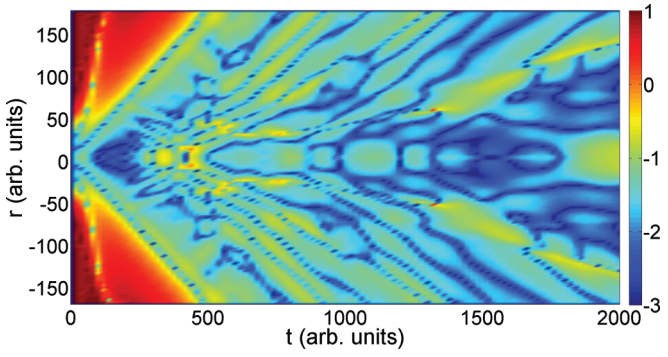

FIG. 5. (Color online) Distribution of $\log_{10}|\log_{10}(|\psi/\psi_{1D}|^2)|$ along a space diagonal to the computational domain is plotted as a function of time. The parameters of the simulation are the same as in Fig. 4.

where a convergent spherical wave reflected from the said mirror formed a focal spot in the center of the image. In the second example, the ψ field is leaking [see Fig. 7(a)] from the well. After that, the remaining part of it becomes a superposition of the bound states of the well, which are excited by the initial Gaussian wavelet. As can be seen in Figs. 7(b)–7(d), these bound states interfere with each other as the wave function evolves over time, forming some oscillating pattern. In both Figs. 6 and 7, there are no apparent reflections from the artificial boundary.

V. CONCLUSION

An exact transparent boundary condition for the 3D time-dependent Schrödinger equation in a rectangular cuboid computational domain has been obtained. It can be easily accommodated in any existing FD scheme, providing an efficient way to describe the wave function freely evolving outwards from the computational domain. This 3D TBC is based on a similar 2D TBC, which was reported earlier [12]. The obtained boundary condition relates the boundary wave function values at the current computational step to (i) boundary values of the wave function at all previous steps and (ii) values of an auxiliary function at the edges and vertices of the computational domain at all previous steps. An interesting feature of the proposed boundary condition is that it involves 2D and 1D evolution of an auxiliary function in the bounding lateral facets and edges of the RCCD, satisfying Schrödinger equations of lower dimensions. Accounting for the edge and vertex contribution is exact in this approach. The validity of the derived boundary

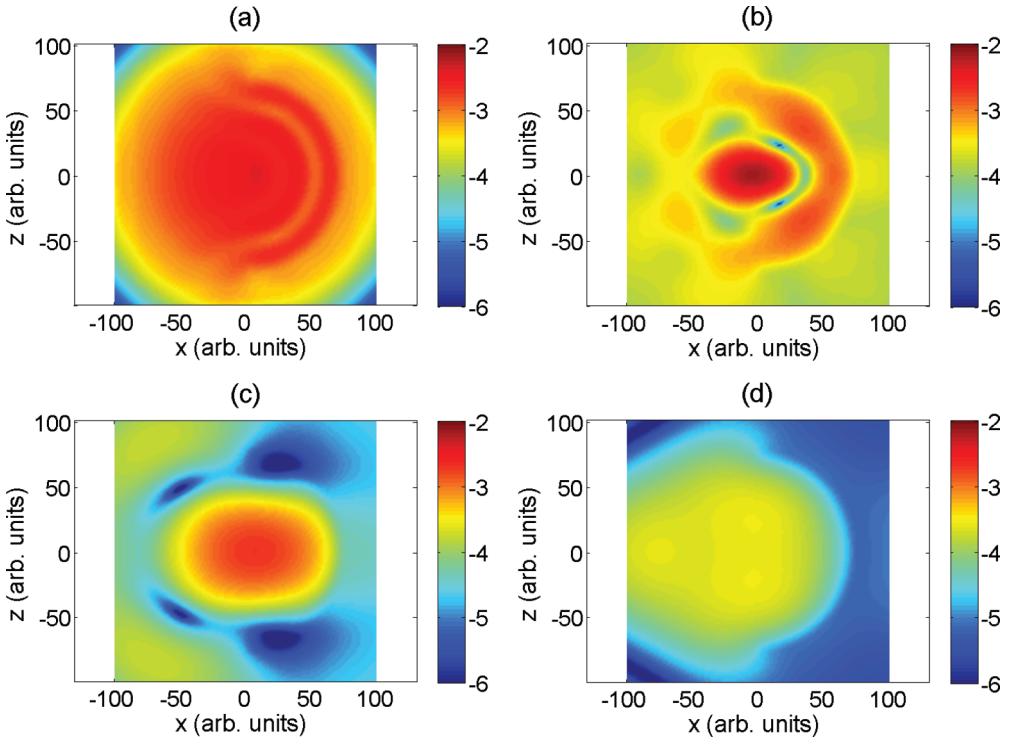

FIG. 6. (Color online) Reflection of a particle off a semispherical barrier with $r_0 = 70$ and $r_1 = 80$. Distributions of $\log_{10}|\psi|^2$ in the (x,z) plane at $y = 0$ are plotted at four different times: (a) −320, (b) −640, (c) −1280, and (d) −1920 arb. units.

condition is demonstrated by numerical experiments with a superposition of Gaussian wavelets evolving in free space as well as by solving some reference quantum potential barrier propagation and scattering problems in 3D space.

There remain some unanswered questions: (i) The numerical stability of the FD scheme utilizing the proposed TBC is to be formally proved, although we have not noticed any numerical instabilities in various numerical experiments

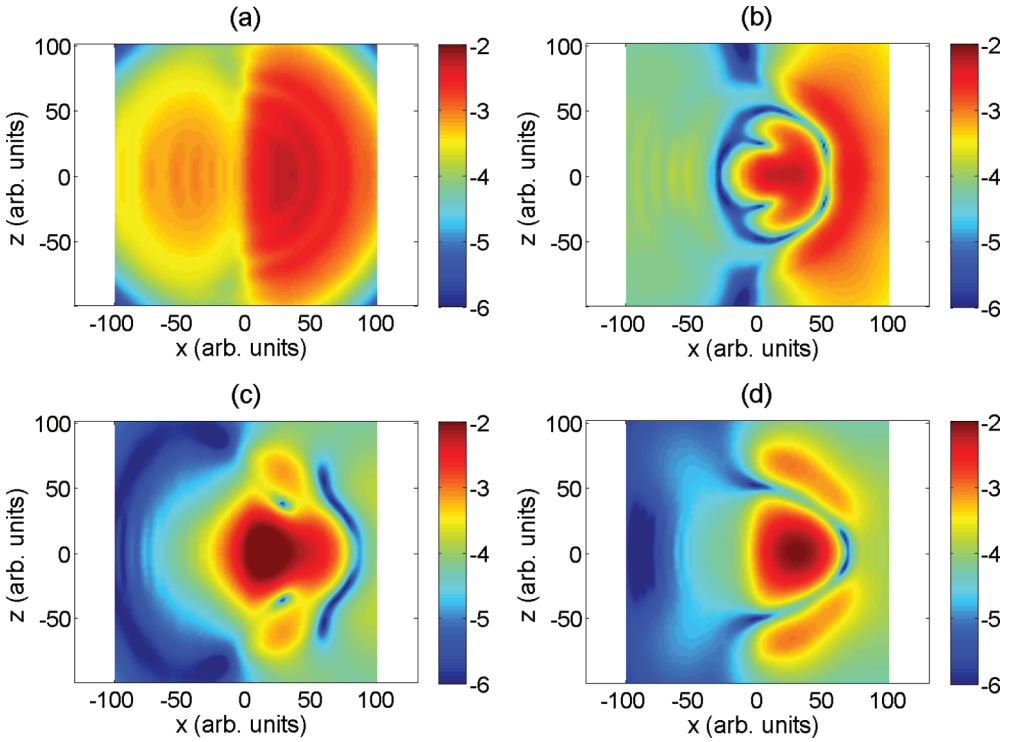

FIG. 7. (Color online) Evolution of wave function in a semispherical potential well with $r_0 = 70$. Distributions of $\log_{10}|\psi|^2$ in the (x,z) plane at $y = 0$ are plotted at four different times: (a) −320, (b) −640, (c) −1280, and (d) −1920 arb. units.

(including those reported in this paper). If it is not unconditionally stable, an unconditionally stable implementation similar to the SDY will be highly desirable. (ii) It is interesting whether the proposed analytical approach involving evolution of an auxiliary function on the boundary of the computational domain can be modified to apply to 3D computational domains other than a RCCD, with one example being a spherical domain. For this to happen, a substitute of Fresnel transform (7) is to be devised.

The TBC proposed in the present paper, as well as one reported in Ref. [12], can be generalized to the Schrödinger equation in a hyperrectangular computational domain in an arbitrary d-dimensional (dD) space. The boundary condition will generally look like that in Eq. (14) but should be formulated on the $2d(d-1)$-dimensional hyperfacets of the hyperrectangle. The auxiliary function Ψ of $2d$ variables will be marching from the nth to $(n+1)$th step on each hyperfacet using TBCs formulated on their $2d(d-1)$ edges. This procedure will involve solution of the free space $(d-1)$D Schrödinger equation. The procedure will need to be repeated recurrently $d-1$ times on the hyperfacets of lower dimension until boundary elements of the dimension 0 (vertices) are reached. At each step, concerning s-dimensional elements, solution of the s-dimensional free space Schrödinger equation will be required in order to extend the auxiliary function Ψ from n to $n+1$. The total number of s-dimensional boundary elements is $E_{ds} = 2^{d-s} d!/s!/(d-s)!$. Each of them will have an associated d-dimensional array with $N^s \times n^{d-s}$ elements that will need to be stored for use in the next computational step. The total number of stored complex numbers at each computational step will be $(N+2n)^d - N^d$. As a result, the memory requirements may be quite significant. The computational complexity of the whole procedure outlined above will be proportional to $P \times N^{2d} + T \times n^d$. The critical point where the boundary condition starts to dominate will be again $n \sim N^2$, like in the 3D case.

The generalization to higher dimensions may be useful for the problems involving multiple noninteracting particles in an external compact potential. In such a case, the particles will be entangled and the evolution of their multiparticle wave function may be of considerable interest.

ACKNOWLEDGMENTS

The authors would like to thank A. V. Vinogradov for the fruitful discussions about the parabolic and Schrödinger equations and their applications. This work was supported in part by the research program of the Physical Science division of the Russian Academy of Sciences—"Laser systems based on new active materials and optics of nano-structured materials," and by the Russian Foundation for Basic Research (RFBR) Grant No. 13-02-01009-a.

[1] J. Crank and P. Nicolson, Proc. Cambridge Philos. Soc. **43**, 50 (1947).
[2] Yu. V. Kopylov, A. V. Popov, and A. V. Vinogradov, Opt. Commun. **118**, 619 (1995).
[3] X. Antoine, A. Arnold, C. Besse, M. Ehrhardt, and A. Schädle, Commun. Comput. Phys. **4**, 729 (2008).
[4] J. Berenger, J. Comput. Phys. **114**, 185 (1994).
[5] V. A. Baskakov and A. V. Popov, Wave Motion **14**, 123 (1991).
[6] A. V. Popov, Radio Science **31**, 1781 (1996).
[7] D. Yevick, T. Friese, and F. Schmidt, J. Comp. Physics **168**, 433 (2001).
[8] K. Boucke, H. Schmitz, and H.-J. Kull, Phys. Rev. A **56**, 763 (1997).
[9] M. Mangin-Brinet, J. Carbonell, and C. Gignoux, Phys. Rev. A **57**, 3245 (1998).
[10] H. Han, D. Yin, and Z. Huang, Numer. Methods Partial Differ. Eq. **23**, 511 (2006).
[11] M. Heinen and H.-J. Kull, Phys. Rev. E **79**, 056709 (2009).
[12] R. M. Feshchenko and A. V. Popov, J. Opt. Soc. Am. A **28**, 373 (2011).
[13] D. W. Peaceman and H. H. Rachford, Jr., J. Soc. Indust. Appl. Math. **3**, 28 (1955).
[14] H. Tal-Ezer and R. Kosloff, J. Chem. Phys. **81**, 3967 (1984).
[15] W. van Dijk, J. Brown, and K. Spyksma, Phys. Rev. E **84**, 056703 (2011).